J. Fluid Mech. (2008), *vol.* 611, *pp.* 283–306. © 2008 Cambridge University Press
doi:10.1017/S0022112008002814 Printed in the United Kingdom

Finite-amplitude river dunes

M. COLOMBINI AND A. STOCCHINO

Dipartimento di Ingegneria delle Costruzioni, dell'Ambiente e del Territorio, Università degli Studi di Genova Via Montallegro 1, 16145 Genova, Italy

(Received 12 October 2007 and in revised form 5 June 2008)

The linear and weakly nonlinear stability of a uniform flow in an infinitely wide open channel with erodible bottom is studied. Under suitable conditions the flow is found to be unstable, leading to the formation of dunes and antidunes. At a linear level, the corresponding regions of existence are presented and compared with experimental data. A weakly nonlinear analysis is then performed in a neighbourhood of the critical conditions for dune and antidune formation. The analysis shows that, for values of the ratio of the shear velocity to the depth-averaged velocity of practical interest, dune bifurcation is supercritical, whereas antidune bifurcation is subcritical. The latter result suggests a possible interpretation of the plane–antidune transition, where plane bed and antidune configurations are observed to coexist for the same values of the flow and the sediment parameters. The supercritical behaviour of the dune bifurcation allows for the prediction of an equilibrium amplitude that successfully compares with the amplitudes measured in laboratory experiments.

1. Introduction

Dunes are, by far, the most common bedforms encountered in rivers, and their dynamics is crucial in many environmental and river engineering problems (ASCE 2002). Antidunes are of lesser practical importance, though of similar conceptual relevance. This justifies the great effort that has been dedicated to the understanding of the physical processes that eventually lead to the formation of these bedforms, even though many questions still remain open (ASCE 2002).

Dunes appear in the so-called lower flow regime (i.e. for small values of the Froude number) and are characterized by downstream propagation and by being almost out of phase with respect to water-surface gravity waves. On the contrary, antidunes occur in the upper flow regime (i.e. for values of the Froude number close to unity) and typically propagate upstream, being almost in phase with free-surface oscillations. In both cases, the main geometrical characteristics of the bedforms scale with the mean flow depth.

The first theoretical contributions on the problem of dune and antidune formation date back to the early 1960s, when the seminal studies of Kennedy (1963) and Reynolds (1965) were published. In these works, the idea that bedforms are the result of a process of instability of the system composed by a uniform flow over an erodible bed was exploited, opening the way to a conspicuous field of research, soon extending from dunes to other river bedforms (e.g. Callander 1969; Sumer & Bakioglu 1984), from altimetric to plano-altimetric morphodynamics (e.g. Ikeda, Parker & Saway 1981; Blondeaux & Seminara 1985), from rivers to lagoon, coastal and marine environments (e.g. Blondeaux 1990; Besio, Blondeaux & Vittori 2006).

https://doi.org/10.1017/S0022112008002814 Published online by Cambridge University Press

Making use of techniques imported from the field of hydrodynamic stability, several analyses were developed in a linear context with the aim of identifying the mechanism that controls dune and antidune instability, thus, defining the region of their existence in the space of the relevant physical parameters (see e.g. Engelund 1970; Smith 1970; Fredsøe 1974; Richards 1980; Coleman & Fenton 2000).

This mechanism is already detectable in the linearized form of the Exner sediment continuity equation, which reveals that a phase-lag between sediment transport and bed topography is required in order to achieve instability. Whether this phase-lag is generated by the flow or the sediment transport or both, has long been discussed.

Regarding the flow, a rotational two-dimensional model is required for the bed shear stress to lead with respect to bed topography (Engelund 1970), even though Coleman & Fenton (2000) have shown that a lag is found also in irrotational models if time derivatives are retained in the momentum equations. Moreover, suspension and sediment inertia are known to produce a further lag between the bottom shear stress and the sediment load (see Parker 1975, and the related discussion).

All these analyses provide a similar overall picture of instability: for given sediment characteristics, as the Froude number F, the instability parameter, is increased above the critical threshold for sediment motion, dunes appear and are then washed out as F is further increased above a second threshold value; antidunes appear when a third threshold is exceeded.

One of the major concerns about linear analyses was that, dealing with infinitesimal, though exponentially growing, disturbances, their ability to predict dune geometry should be limited to the very initial stage of formation (Coleman & Melville 1996). Since nonlinearity is known to play a role in dune further development towards an equilibrium amplitude, it was inferred that information pertaining to the initial stage had little or nothing to do with the finite-amplitude development of dunes. Moreover, the output of linear analyses is limited to the definition of an unstable region in the parameter space and to an indication on the wavelength and celerity of the most unstable disturbance of the bottom. No information is gathered on dune amplitude at a linear level.

Although the results of most of these analyses compare satisfactorily with laboratory and field observations, an uncomfortably high degree of uncertainty remained (ASCE 2002), in particular for the delicate transition between dunes, plane bed and antidunes.

For these reasons, the problem of flow over fixed (inerodible) bedform shapes has received intense attention, through detailed flow measurements and numerical simulations (see Best 2005, and references therein). In particular, near-bed turbulence and flow separation on the lee side of dunes have been charged as the major agents in determining dune geometry (Coleman *et al.* 2006), even though debate still exists as to the nature and cause of river dunes with low-angle leesides, where separation is likely to be absent (Best & Kostaschuk 2002). In addition, the numerical results by Tjerry & Fredsøe (2005) suggest that streamline curvature could be as important as flow separation in the prediction of the fully developed geometry of dunes. Further contributions have concentrated on numerical models of flow over an erodible bed based on more or less refined closures to simulate flow separation (Giri & Shimizu 2006).

Here, we attempt a different approach, hopefully able to clarify the role of nonlinearity, at least for low-amplitude dunes. Colombini (2004) has proposed a linear analysis of dune and antidune formation, showing how a careful modelling of the flow field and of the sediment transport leads to a more reliable formulation of the linear problem in the absence of suspension. Following ideas well-established

https://doi.org/10.1017/S0022112008002814 Published online by Cambridge University Press

in the field of hydrodynamic instability (Stuart 1971), a weakly nonlinear stability theory based on the same flow and sediment transport model is formulated herein.

As opposed to other bedforms (e.g. bars, see Colombini *et al.* 1987; Schielen, Doelman & de Swart 1993), few attempts at investigating the weakly nonlinear regime of dune instability can be found in the literature. The role of second-order interactions in defining the dune shape has been outlined by Fredsøe (1974), whereas Ji & Mendoza (1997) have investigated the weakly nonlinear second-order correction of the growth rate. In the following, it will be shown how, extending the analysis to the third order, a Landau–Stuart amplitude equation is eventually recovered, which describes the time evolution of a perturbation on a slow time scale at the onset of instability.

Before entering into the details of our analysis, some further considerations on the nature of the instability process that leads to dune and antidune formation may be helpful. No formal proof has been provided yet to ascertain whether the character of the instability is absolute or convective. We recall that instability is convective provided an initial small perturbation localized in space is convected downstream, whereas it is absolute if the perturbation spreads both upstream and downstream as time grows.

The present weakly nonlinear analysis is definitely appropriate in the latter case, since the Landau–Stuart equation describes well the evolution in time of a monochromatic spatially periodic perturbation. If the process of instability is convective, as in the case of bars (Federici & Seminara 2003), both spatial and temporal modulations of the nonlinear solution have to be considered. Moreover, in a neighbourhod of the critical conditions, a group of perturbations characterized by wavenumbers close to the critical one is unstable and, owing to dispersion of this wave group, a spatial modulation will occur.

It is well known that, if a slow spatial scale is introduced in the analysis in addition to the slow time scale, then a Ginzburg–Landau amplitude equation is eventually obtained. Before embarking on the derivation of the latter, we felt it necessary to verify to what extent a weakly nonlinear approach may be suitable for interpreting the gross features of the nonlinear dynamics of dunes and antidunes.

The paper proceeds as follows: in § 2, the problem of flow in an infinitely wide channel with erodible bottom is formulated. Section 3 is devoted to the solution of the linear problem and § 4 to a discussion of the main results of the linear analysis. The weakly nonlinear analysis is performed in § 5 and the results on dune geometry are analysed and compared with experimental measurements of dune amplitude in § 6. Section 7 concludes the paper with some final remarks.

2. Formulation of the problem

Let us consider a uniform turbulent free surface flow in a infinitely wide straight channel. The triplet composed by the fluid density ρ, the mean friction velocity u_f^* and depth D^* of the unperturbed uniform flow has been used for non-dimensionalization. In the following, a star superscript denotes a dimensional variable.

In the sloping Cartesian coordinate system (x, y) sketched in figure 1, the dimensionless unsteady Reynolds and continuity equations are:

$$U_{,t} + UU_{,x} + VU_{,y} + P_{,x} - gD^* \sin\alpha/(u_f^*)^2 - T_{xx,x} - T_{xy,y} = 0, \tag{2.1}$$

$$V_{,t} + UV_{,x} + VV_{,y} + P_{,y} + gD^* \cos\alpha/(u_f^*)^2 - T_{xy,x} - T_{yy,y} = 0, \tag{2.2}$$

$$U_{,x} + V_{,y} = 0, \tag{2.3}$$

https://doi.org/10.1017/S0022112008002814 Published online by Cambridge University Press

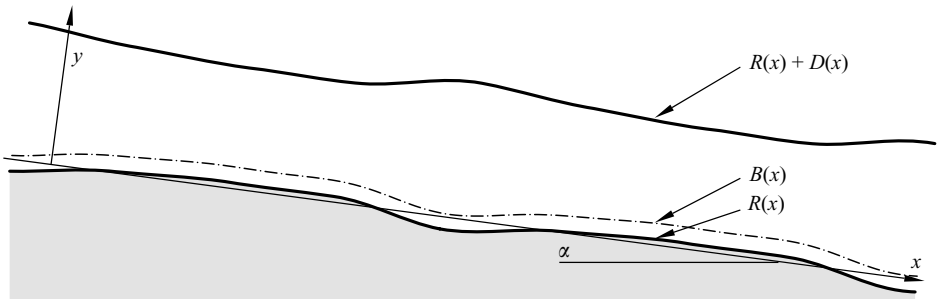


FIGURE 1. Sketch of flow configuration.

where $\boldsymbol{U}=(U,V)$ is the local velocity vector averaged over turbulence, P is the pressure, $\boldsymbol{T}=\{T_{ij}\}$ is the two-dimensional Reynolds stress tensor, g is the acceleration due to gravity and α is the angle formed by the x-axis with respect to the horizontal.

Moreover, we define a non-dimensional conductance coefficient C as the ratio between the unperturbed depth-averaged velocity $\overline{U}^*$ and the mean friction velocity u_f^*, which can be related to the flow depth and the sediment diameter d_s^* through the Keulegan equation (ASCE 1963) for fully rough turbulent flow:

$$C=\frac{\overline{U}^*}{u_f^*}=\frac{1}{\kappa}\ln\left(\frac{11.09D^*}{2.5d_s^*}\right), \tag{2.4}$$

where κ is the von Kármán constant, taken as 0.4, and the roughness height has been set as $2.5d_s^*$ after Engelund & Hansen (1967). Note that C is related to the dimensional Chézy coefficient χ and to the non-dimensional Darcy–Weisbach friction coefficient f through the following relathionships:

$$C=\frac{\chi}{\sqrt{g}}=\sqrt{\frac{8}{f}}, \tag{2.5}$$

Assuming the mean bed slope $S=\tan\alpha$ to be small, we can safely set:

$$\sin\alpha\simeq\tan\alpha=S,\qquad \cos\alpha\simeq 1, \tag{2.6}$$

so that the gravity terms in the momentum equations (2.1)–(2.2) become, respectively:

$$gD^*\sin\alpha/(u_f^*)^2=SC^2/F^2,\qquad gD^*\cos\alpha/(u_f^*)^2=C^2/F^2, \tag{2.7}$$

where $F=\overline{U}^*/\sqrt{gD^*}$ is the Froude number.

The flow domain is bounded by the curves $y=R(x,t)$ and $y=R(x,t)+D(x,t)$, with D the local flow depth. The lower boundary is set at the reference level R, where the velocity is assumed to vanish.

Having denoted as $\boldsymbol{n}$ and $\boldsymbol{t}$ the unit vectors normal and tangential to each boundary, respectively, the kinematic and dynamic boundary conditions to be associated with (2.1)–(2.3) are:

$$-R_{,t}+\boldsymbol{U}\cdot\boldsymbol{n}=0,\quad \boldsymbol{U}\cdot\boldsymbol{t}=0\quad (y=R), \tag{2.8}$$

$$-(R+D)_{,t}+\boldsymbol{U}\cdot\boldsymbol{n}=0,\qquad \boldsymbol{n}\cdot\boldsymbol{T}\cdot\boldsymbol{t}=0,\qquad \boldsymbol{n}\cdot\boldsymbol{T}\cdot\boldsymbol{n}=0\qquad (y=R+D). \tag{2.9}$$

The following transformation of variables:

$$\eta=\frac{y-R(\xi,\tau)}{D(\xi,\tau)},\qquad \xi=x,\qquad \tau=t, \tag{2.10}$$

is then employed to map the domain shown in figure 1 into a rectangular domain.

https://doi.org/10.1017/S0022112008002814 Published online by Cambridge University Press

In order to close the above formulation the Boussinesq closure is used, which is:

$$T_{ij} = \nu_T(U_{i,j} + V_{j,i}). \tag{2.11}$$

The eddy viscosity ν_T is evaluated by means of the mixing-length approach, hence:

$$\nu_T = l^2 U_{,y}\,, \qquad l = DL(\eta), \qquad L(\eta) = \kappa(\eta + \eta_r)(1-\eta)^{1/2}. \tag{2.12}$$

For a uniform flow, the algebraic function $L(\eta)$ produces a parabolic profile for the eddy viscosity and, consequently, the logarithmic law of the wall, with η_r being the dimensionless distance between the reference level and the average bed level.

Sediments are assumed to be transported as bedload only, following the approach adopted by Colombini (2004). Hence, sediment transport is confined within a thin saltation layer adjacent to the bottom, such that the flow above is the same as if the bed were fixed. Hence, the intensity of the sediment transport is determined by the shear stress acting at the interface between the saltation layer and the clear water.

Based on the above considerations, the Exner equation imposing mass conservation of sediments takes the form:

$$FR_{,t} + Q_0 \Phi_{,x} = 0, \qquad Q_0 = C\frac{d_s\sqrt{(s-1)d_s}}{(1-p_s)}, \tag{2.13}$$

where Φ is the dimensionless form of the sediment transport capacity per unit width and s and p_s are relative density and porosity of the sediment, respectively.

The function Φ is known to depend on a dimensionless form of the bed shear stress acting on the bedload layer, namely the Shields stress θ_b. Results are only moderately affected by the choice of a particular form for the function Φ. In the following, the classical Meyer-Peter & Müller (1948) formula:

$$\Phi = A_m(\theta_b - \theta_c)^{3/2} \qquad (\theta_b \geqslant \theta_c), \tag{2.14}$$

has been employed, where θ_c is the critical Shields stress for incipient motion. The values of θ_c and A_m have been set equal to 0.0495 and 3.97, respectively, in accordance with the corrections proposed by Wong & Parker (2006) in their revisitation of the work of Meyer-Peter & Müller (1948). In addition, the effect of gravity on the grain motion is included by setting the critical Shields stress θ_c equal to:

$$\theta_c = 0.0495 - \mu(S - R_{,x}), \tag{2.15}$$

where μ is a dimensionless constant set equal to 0.1 after Fredsøe (1974).

As for the saltation layer, its thickness is known to scale with the sediment grain size d_s and can be defined as:

$$h_b = (1 + h_s)d_s, \tag{2.16}$$

where h_s is the average maximum saltation height of a grain positioned above the bed, scaled by the grain diameter. The dependence of the latter on the flow intensity is expressed by the relationship:

$$h_s = A_b\left(\frac{\theta_r - \theta_c}{\theta_c}\right)^m \qquad (\theta_r \geqslant \theta_c), \tag{2.17}$$

where θ_r is the value of the Shields stress evaluated at the reference level and the constants A_b and m have been set equal to 1.42 and to 0.64, respectively, based on a regression on the experimental data of Sekine & Kikkawa (1992) and Lee & Hsu (1994). These values differ slightly from those adopted by Colombini (2004), since a procedure similar to that suggested by Wong & Parker (2006) has been applied to the experimental data in order to compensate for sidewall effects.

https://doi.org/10.1017/S0022112008002814 Published online by Cambridge University Press

Finally, the level at which the Shields stress θ_b is evaluated is:

$$y = B = R + \left(h_b + \frac{d_s}{12}\right) D, \qquad \eta = \eta_b = \left(h_b + \frac{d_s}{12}\right), \tag{2.18}$$

where the term $d_s/12$ accounts for the distance between the reference level and the top of the grains composing the bed.

3. Linear theory

The linearization procedure follows closely that described in Colombini (2004) and Colombini & Stocchino (2005) and is only briefly summarized in the following for the sake of clarity, since most of the notations introduced herein are later used in the weakly nonlinear analysis.

The problem formulated in the previous section is solved in terms of normal modes, so that a generic perturbed quantity G is written as:

$$G(\xi, \eta, \tau) = G_0(\eta) + \epsilon G_1(\xi, \eta, \tau), \tag{3.1}$$

$$G_1(\xi, \eta, \tau) = A G_{11}(\eta) \exp[ik(\xi - \Omega\tau)] + \text{c.c.}, \tag{3.2}$$

where ϵ is a small parameter, k and Ω are wavenumber and complex growth rate of the perturbation, respectively, and *c.c.* stands for complex conjugate. The quantity A represents, in the present context, an arbitrary factor.

Substituting the above expansion into the governing equations, boundary conditions and turbulence closure and collecting terms of the same order of magnitude in ϵ, the following differential problems arise. Note that, for convenience, the tangential (T_t) and normal (T_n) components of the stress acting on surfaces at constant η are introduced below, the latter including the role of pressure.

3.1. $O(\epsilon^0)$

At leading order, integration of the system of differential equations yields a linear distribution of shear stress and the classic velocity logarithmic law:

$$U_0 = \frac{1}{\kappa} \ln\left(\frac{\eta + \eta_r}{\eta_r}\right), \tag{3.3}$$

and, by direct integration, the depth-averaged speed is obtained:

$$U_0 = \frac{U^*}{u_f^*} = C = \frac{1}{\kappa}\left[\ln\left(\frac{1 + \eta_r}{\eta_r}\right) - 1\right], \tag{3.4}$$

which can be used to relate the coefficient C to η_r. Consistent with (2.4), the distance η_r of the reference plane from the average bed elevation is found to be roughly equal to one-thirtieth of the non-dimensional roughness height, or, alternatively, one-twelfth of the non-dimensional sediment diameter d_s. Furthermore, C is related to the Froude number F and to the unperturbed slope S_0 through the relationship:

$$C = \frac{F}{\sqrt{S_0}}, \tag{3.5}$$

which expresses the well-known balance between friction and fluid weight in a uniform flow.

Exner equation (2.13) does not produce any additional information, since, under uniform flow conditions, the bed experiences neither aggradation nor degradation.

https://doi.org/10.1017/S0022112008002814 Published online by Cambridge University Press

The following relationships hold:

$$\theta_{r0} = \frac{S_0}{(s-1)d_s}, \qquad \theta_{b0} = \theta_{r0}(1-\eta_b), \qquad \theta_{c0} = 0.0495 - \mu S_0, \tag{3.6}$$

$$\Phi_0 = 3.97(\theta_{b0} - \theta_{c0})^{3/2}, \qquad Q = \frac{3}{2}\frac{Q_0\Phi_0}{\theta_{b0} - \theta_{c0}}. \tag{3.7}$$

Note that the thickness of the saltation layer has not been perturbed so that the level η_b depends only on the basic flow quantities θ_{r0} and θ_{c0} through (2.16)–(2.18).

3.2. $O(\epsilon^1)$

At the linear level, after some manipulation, a system of ordinary differential equations for the unknown vector $\boldsymbol{Z}_{11} = (U_{11}, V_{11}, T_{t11}, T_{n11})^T$ is eventually obtained and can be written in the general form:

$$\mathscr{L}_{11}\boldsymbol{Z}_{11} - D_{11}\boldsymbol{D}_{11} - R_{11}\boldsymbol{R}_{11} = \{0\}, \tag{3.8}$$

where the linear differential operator $\mathscr{L}_{11}$ and the vectors $\boldsymbol{D}_{11}$ and $\boldsymbol{R}_{11}$ are given in Appendix A, D_{11} and R_{11} are treated as parameters to be determined.

The solution of the linear differential system (3.8) is:

$$\boldsymbol{Z}_{11} = c_{11}^{(1)}\boldsymbol{Z}_{11}^{(1)} + c_{11}^{(2)}\boldsymbol{Z}_{11}^{(2)} + D_{11}\boldsymbol{Z}_{11}^{(D)} + R_{11}\boldsymbol{Z}_{11}^{(R)}. \tag{3.9}$$

Thus, $\boldsymbol{Z}_{11}$ is expressed as a linear combination of two linearly independent solutions of the homogeneous initial-value problem

$$\mathscr{L}_{11}\boldsymbol{Z}_{11}^{(1,2)} = 0, \tag{3.10}$$

which satisfy the boundary conditions at the lower boundary, plus particular solutions of the non-homogeneous differential systems:

$$\mathscr{L}_{11}\boldsymbol{Z}_{11}^{(D)} = \boldsymbol{D}_{11}, \qquad \mathscr{L}_{11}\boldsymbol{Z}_{11}^{(R)} = \boldsymbol{R}_{11}, \tag{3.11}$$

again satisfying the lower boundary conditions. Without loss of generality, the constants $c_{11}^{(1)}$ and $c_{11}^{(2)}$ are chosen so as to represent the amplitude of the perturbed tangential and normal stresses at the reference level, respectively.

Making use of the relationships (2.14)–(2.18), linearization of the sediment continuity equation (2.13) yields:

$$\Omega F R_{11} - Q(\theta_{r0}T_{t11b} - \mathrm{i}k\mu R_{11}) = 0, \tag{3.12}$$

where T_{t11b} is the perturbation of the shear stress evaluated at the level η_b.

Equation (3.12) shows that instability is the result of a balance between the destabilizing effect of the shear stress and the stabilizing role of gravity. Using the splitting (3.9) in the linearized boundary conditions at the free surface (2.9) and in the Exner equation (3.12), the following complex algebraic homogeneous system is eventually obtained:

$$\boldsymbol{U}_{11}\cdot\boldsymbol{C}_{11} = \{0\}, \qquad \boldsymbol{C}_{11} = \left(c_{11}^{(1)}, c_{11}^{(2)}, D_{11}, R_{11}\right)^T, \tag{3.13}$$

where the matrix $\boldsymbol{U}_{11}$ is given in Appendix A. Note that, owing to the coupling between flow and sediment transport, all the coefficients of $\boldsymbol{U}_{11}$ implicitly depend on the complex growth rate Ω.

A non-trivial solution of the system is then obtained for the particular values of Ω (the eigenvalues) that make the determinant of $\boldsymbol{U}_{11}$ vanish. The constants $\boldsymbol{C}_{11}$, and therefore the eigenfunctions (3.9), are readily calculated from (3.13) setting R_{11} equal to a half, so that ϵA represents the amplitude of the bed perturbation.

https://doi.org/10.1017/S0022112008002814 Published online by Cambridge University Press

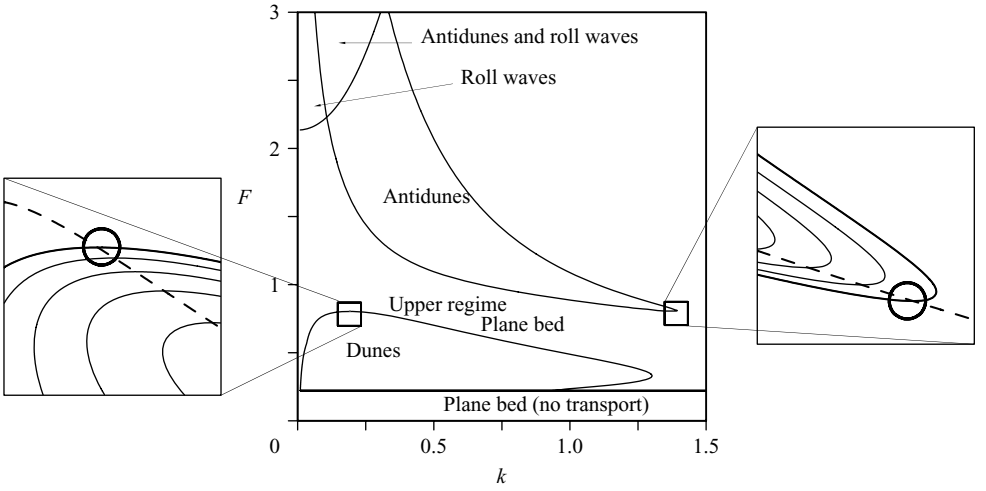


FIGURE 2. Regions of instability for dunes, antidunes and roll waves; $C = 20$, $f = 0.02$. The dashed lines in the close-up pictures correspond to the lines of maximum growth rate.

4. Linear theory: results

The behaviour of the eigenvalues of the linear problem has been extensively investigated by Colombini & Stocchino (2005). In the following, their main results are briefly summarized and a more detailed comparison with the experimental data is performed.

Three separate eigenvalues display unstable regions in the $(k - F)$ space (see figure 2): two of them can be readily associated with the formation of dunes and antidunes, while the third describes the instability of fast sediment waves that appear at high Froude numbers (i.e. $F \geqslant 2$) associated with the presence of roll-waves. The antidune mode is characterized by a small negative celerity (upstream propagation) while the dune mode propagates downstream (positive celerity). The free surface and the bed oscillations are found to be approximately in phase for antidunes and out of phase for dunes, with a small lag coherent with the corresponding direction of migration.

For each value of the coefficient C, two critical points can be identified in the stability plot, say (k_{cd}, F_{cd}) and (k_{ca}, F_{ca}), which are encircled in the close-ups in figure 2. They identify the onset of instability for each mode, since, as the Froude number equals F_{cd} (F_{ca}), the basic plane bed solution loses stability, and periodic perturbations characterized by wavenumber k_{cd} (k_{ca}), which represent the bedform, grow. The critical Froude number for roll-wave instability F_{cr} is found in the long-wave limit $k_{cr} \to 0$.

At a linear level, no dune-like disturbances are unstable above F_{cd}, while no unstable disturbances are found below F_{ca} and F_{cr} for the antidune and roll-wave modes, respectively. On the basis of the critical Froude numbers F_{cd}, F_{ca} and F_{cr}, a map of the linear regions of instability for dunes, antidunes and roll-waves can thus be obtained in the $(C - F)$ space, as shown in figure 3.

Five distinct regions can be identified in the plot. The lowermost region is characterized by values of the unperturbed Shields stress lower than the threshold for sediment motion and the bed is therefore plane; as soon as the critical threshold for motion is exceeded, dunes appear in the second region, which is bounded from above

https://doi.org/10.1017/S0022112008002814 Published online by Cambridge University Press

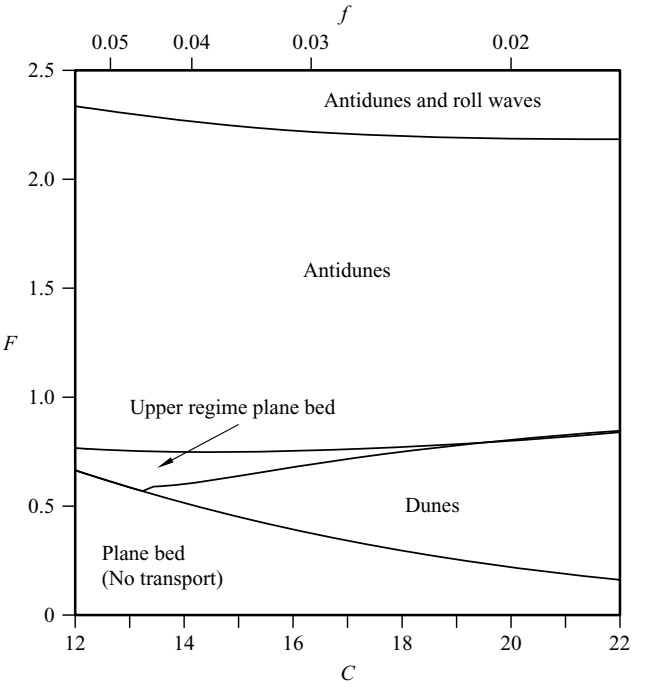


FIGURE 3. Theoretical regions of linear instability in the $(C - F)$ space.

by the critical Froude number for dune formation F_{cd}. It must be noted that the latter decreases with decreasing C, while the threshold for sediment motion increases, so that the two curves cross at a value of C of about 13. The region bounded from below by F_{cd} and from above by F_{ca} is the upper regime plane bed region, which marks the transition between dunes and antidunes. Again, the two curves practically coincide for values of C larger of 19. Finally, the antidune region is found above F_{ca}, while antidune and roll-wave disturbances are both simultaneously unstable if the last threshold F_{cr} is exceeded.

Although the overall pattern of instability described in figure 2 is well-known since the theoretical work of Kennedy (1963), some interesting information emerges from the analysis of the present theoretical results: (i) the dune region reduces in amplitude as C decreases, so that no dunes are expected to form for $C < 13$, a value which corresponds to gravel; (ii) the plane bed mode with active sediment transport is confined within a narrow band that tends to disappear as C increases; (iii) as a consequence, dune and antidune modes turn out to coexist for $C > 19$ (fine sand); (iv) the appearance of the unstable roll-wave mode, which is hidden by the quasi-steady approximation adopted in most analyses, provides a possible limiting mechanism for antidune formation at high Froude numbers.

The main purpose of the present contribution is to investigate dune and antidune instabilities and their transition towards plane bed configurations. Therefore, the analysis of the mutual interactions between antidunes and roll-waves described at the latest point above is beyond our present scope.

In the following, the proposed theoretical existence criteria are compared with experimental observations. The most comprehensive collection of flume experiments concerning finite-amplitude bedforms is the Fort Collins data set of Guy, Simons &

https://doi.org/10.1017/S0022112008002814 Published online by Cambridge University Press

Richardson (1966), which covers a wide range of grain sizes, flow depths and Froude numbers. Among the variety of bedforms observed during the experiments, data classified as dune, plane bed, antidune and transitional are all relevant for the present analysis.

As noted by Engelund (1970), the comparison of the results of the stability analysis with experimental observations is difficult because data are collected when bedforms have reached a fully developed state, whereas the starting point for the stability analysis is the basic state, i.e. a uniform flow in an infinitely wide plane bed channel. The presence of bedforms induces considerable changes of the flow resistance due to form drag, so that, even at a constant discharge, slope and depth of the final equilibrium state could be considerably different from the initial plane ones. In this regard, some of the experiments of Guy *et al.* (1966) were conducted keeping constant both the flow discharge and the flow depth and letting the slope adjust itself to the increased resistance due to the presence of bedforms so that the Froude number remained unchanged. For some other runs, however, the slope was kept constant either by adjusting the flow depth or the discharge, or both.

In any case, since all the information collected by Guy *et al.* (1966) is relative to the final experimental configurations, an equivalent uniform flow has been sought to the one characterized, in the same channel, by the same flow depth H^* and area velocity V^* as measured at the end of the run, thus disregarding information on the measured slope and friction coefficient. In other words, following a well-established approach that dates back to Meyer-Peter & Müller (1948), the measured slope of the energy grade line has been partitioned into one related to form resistance and another associated with skin friction, only the latter being of significance for the identification of the basic flow corresponding to each experiment.

Other difficulties in the interpretation of the experimental results arise from the presence of smooth sidewalls in the experiments and by the heterogeneity of the sediment mixtures used, both affecting skin friction. To overcome these difficulties a procedure similar to that proposed by Wong & Parker (2006), which ultimately led to the modified version of the Meyer-Peter & Müller relationship (2.14), has been applied to each experimental run.

It may be useful at this point to briefly summarize the salient assumptions on which this procedure is based.

Starting from the Darcy–Weisbach equation (Rouse 1946):

$$V^* = \sqrt{\frac{8gr^*S}{f}}, \tag{4.1}$$

where f is the total Darcy–Weisbach friction coefficient and r^* is the hydraulic radius, the cross-section is partitioned into a bed and a wall region, each characterized by the same value of the energy slope S and mean velocity V^* (Vanoni & Brooks 1957).

If (4.1) is then applied to each region we obtain:

$$\frac{r_b^*}{f_b} = \frac{r_w^*}{f_w} = \frac{r^*}{f}, \tag{4.2}$$

where the subscripts b and w refer to the bed and wall region, respectively.

The friction coefficients of the wall and bed region (f_w, f_b) are then related to the corresponding hydraulic radii through the Keulegan equations (ASCE 1963) for

https://doi.org/10.1017/S0022112008002814 Published online by Cambridge University Press

smooth and rough flow, respectively:

$$\sqrt{\frac{8}{f_w}} = \frac{1}{\kappa}\ln\left(\frac{R_w\sqrt{f_w}}{3.41}\right), \qquad \sqrt{\frac{8}{f_b}} = \frac{1}{\kappa}\ln\left(\frac{11.09r_b^*}{k_s^*}\right), \tag{4.3}$$

where $R_w = Rr_w^*/r^*$, R is the Reynolds numbers computed by using a characteristic length of $4r^*$, and the roughness height k_s^* has been set equal to $2.5d_{50}^*$ in analogy with (2.4).

Finally, water continuity applied to the case of a rectangular cross-section with wetted perimeters B^* and $2H^*$ for the bed and wall regions, respectively, yields:

$$r^* = \frac{B^*r_b^* + 2H^*r_w^*}{B^* + 2H^*}. \tag{4.4}$$

For any given value of the depth-averaged velocity U^* and of the flow depth H^*, the system composed by (4.2)–(4.4) constitutes an implicit closed set in the unknowns f, f_w, f_b, r_w^* and r_b^*, and can be solved iteratively.

Substitution of the total friction factor f into (4.1) gives an estimate of the slope S of the energy gradient line due to skin friction alone. Moreover, once the hydraulic radius of the bed region r_b^* is known, the corresponding plane-bed shear velocity u_b^* as well as the coefficient C_b can been evaluated as:

$$u_b^* = \sqrt{gr_b^*S}, \qquad C_b = \frac{V^*}{u_b^*} = \sqrt{\frac{8}{f_b}}. \tag{4.5}$$

The final step in the determination of the basic state to be associated with the experimental run consists in setting the undisturbed flow depth D^* in our analysis equal to r_b^*, so that u_b^* devolves to u_f^*, V^* to $\overline{U}^*$ and C_b to C. The shear stress at the bed then becomes equal in the two configurations, which also share the same slope S. Note that, by this choice, the bed hydraulic radius r_b^* takes the role of the characteristic vertical length scale of the flow and it is therefore employed in the process of non-dimensionalization of the height and wavelength of the bedforms. The Froude number to be associated with each experimental run is augmented by this procedure with respect to its measured value, a necessary condition for (3.5) to hold for both flows.

The $(C - F)$ pairs obtained for each experiment of Guy *et al.* (1966) following the above procedure have been superimposed on the theoretical regions of instability in figure 4.

Furthermore, in order to estimate the relevance of suspended sediment transport in the experiments, data have been classified on the basis of the Van Rijn (1984*a*) criterion. Data exceeding the threshold for incipient suspension are shown in grey in figure 4.

The comparison of the theoretical regions of instability with the experiments of Guy *et al.* (1966) shows that the dune regime is predicted with satisfactory accuracy. All the dune runs (circles) fall inside the predicted region and, in particular, the lower boundary separates quite well dunes from no-transport plane bed data (upper triangles). The upper boundary of the dune regime lies among experimental data of the upper flow regime plane bed (upper triangles) and transitional bedforms (lower triangles), the latter being defined by Guy *et al.* (1966) as a 'category for flows that mold bedforms ranging from those typical of the lower flow regime (dunes) to those typical of the upper flow regime (plane bed, antidunes).'

https://doi.org/10.1017/S0022112008002814 Published online by Cambridge University Press

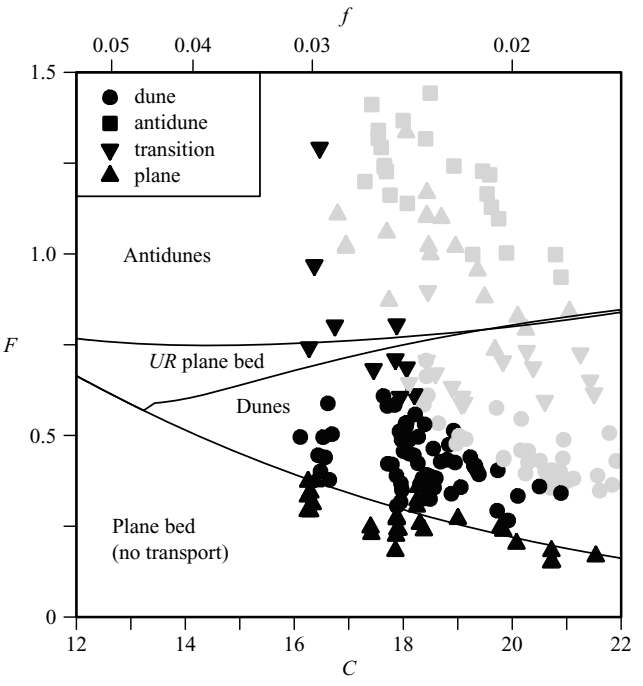


FIGURE 4. Theoretical regions of instability for dunes and antidunes compared with the experimental data of Guy *et al.* (1966). Grey symbols indicate data exceeding the threshold for incipient suspension.

Moreover, as C decreases, the experimental dune runs exhibit a general trend following the predicted tendency for the dune region to reduce in amplitude, which is in agreement with dunes hardly being observed for grain sizes larger than 5 mm (Carling, Richardson & Ikeda 2005). As C increases, the boundary between (transitional) dunes and the upper regime plane bed seems to be slightly overestimated by the theory (see also Carling & Shvidchenko 2002). This may be due to the effect of suspended sediment transport, which has been neglected in the present analysis. Although most of the dune experiments are characterized by negligible suspension according to the Van Rijn (1984*a*) criterion, the number of experimental points exceeding the threshold for suspension clearly increases with C.

The latter consideration also applies to the antidune regime, where certainly suspension plays a more crucial role. If, on one hand, the choice of neglecting suspension has the merit of showing that antidunes can develop also in gravel beds (Colombini 2004), on the other hand, it has the obvious flaw of eliminating a well-known stabilizing effect from the analysis. The inclusion of a suspended load is expected to raise the value of F_{ca} (Engelund 1970) and to lower the value of F_{cd} (Engelund & Fredsøe 1974) as the Shields stress θ exceeds the threshold value θ_s (Van Rijn 1984*a*). In this regard, the regions of instability depicted in figures 3 and 4 can be thought of as the slice at $\theta \leqslant \theta_s$ of a more complex diagram in the three-dimensional space $(C, F, \theta/\theta_s)$ where the experimental data are actually scattered.

A close inspection of the experimental runs concerning the upper flow regime reveals that both antidune and plane bed solutions are observed for similar Froude numbers in the range $0.9 < F < 1.2$, so that a net separation between the two regimes

https://doi.org/10.1017/S0022112008002814 Published online by Cambridge University Press

is hardly detectable in terms of Froude number. Although the inclusion of suspension can, in principle, modify the value of F_{ca}, no explanation can be found at a linear level for this overlapping. We postpone to the weakly nonlinear analysis a possible interpretation of this observed behaviour.

Finally, the fact that transitional bedforms appear close to the critical curve F_{cd}, while finite-amplitude dunes are found for lower values of the Froude number suggests that the bedform amplitude increases with the distance from F_{cd}, which is consistent with the weakly nonlinear expansion that will be presented in the following.

5. Weakly nonlinear theory

We intend to investigate the weakly nonlinear evolution of the perturbations of the flow-bed system in a neighbourhood of the points (k_{cd}, F_{cd}) and (k_{ca}, F_{ca}) shown in figure 2. We then define:

$$F = F_c(1 + \epsilon^2 F_2), \qquad k = k_c, \tag{5.1}$$

where the subscript c indicates either of the two critical points and F_2 is a dummy parameter that takes the value of ± 1.

In order to investigate the nonlinear behaviour of the system we employ a multiscale perturbation technique and define a 'slow' time scale T such that:

$$T = \epsilon^2 \tau, \qquad \frac{\partial}{\partial \tau} \to \frac{\partial}{\partial \tau} + \epsilon^2 \frac{\partial}{\partial T}. \tag{5.2}$$

Nonlinearity gives rise to interactions between the fundamental and itself that lead to the generation of higher harmonics. Following the above cascade process, the fundamental is reproduced at third order. Hence, to prevent the occurrence of secular terms, the slow time dependence of the amplitude of the fundamental must also produce a contribution at the same order.

We then expand the solution in the form:

$$G(\xi, \eta, \tau, T) = G_0 + \epsilon G_1 + \epsilon^2 G_2 + \epsilon^3 G_3, \tag{5.3}$$

and collect terms at the various order of approximation in ϵ.

5.1. $O(\epsilon^1)$

At the linear level, the structure of the solution is analogous to (3.2):

$$G_1 = A(T) G_{11} \exp[\mathrm{i} k_c(\xi - \Omega_c \tau)] + \text{c.c.}, \tag{5.4}$$

where the complex function $A(T)$ is now a 'slowly varying' function of time to be determined.

The differential system (3.8) is recovered, with $\Omega = \Omega_c$ and $k = k_c$, and its solution proceeds as described in § 3. As expected, no information is gathered on the amplitude A at this level of approximation.

5.2. $O(\epsilon^2)$

The structure of the solution at the next order follows from an analysis of the interaction of the fundamental with itself and considering (5.1):

$$G_2 = \{A^2 G_{22} \exp[2\mathrm{i} k_c(\xi - \Omega_c \tau)] + \text{c.c.}\} + A A^* G_{20} + F_2 G_{20F}. \tag{5.5}$$

Three separate differential problems are then obtained at this order, the solutions of which follow a slightly different procedure. We start to form the 22-system which

https://doi.org/10.1017/S0022112008002814 Published online by Cambridge University Press

can be written as:

$$\mathscr{L}_{22}\boldsymbol{Z}_{22} - D_{22}\boldsymbol{D}_{22} - R_{22}\boldsymbol{R}_{22} = \boldsymbol{P}_{22}, \tag{5.6}$$

where the linear differential operator $\mathscr{L}_{22}$ is obtained from $\mathscr{L}_{11}$ substituting k with $2k_c$. Applying the same substitution to $\boldsymbol{D}_{11}$ and $\boldsymbol{R}_{11}$ leads to the vectors $\boldsymbol{D}_{22}$, $\boldsymbol{R}_{22}$. Finally, the vector $\boldsymbol{P}_{22}$ is a lengthy function of η given in Appendix B.†

We then expand the solutions as in (3.9) obtaining:

$$\boldsymbol{Z}_{22} = c_{22}^{(1)}\boldsymbol{Z}_{22}^{(1)} + c_{22}^{(2)}\boldsymbol{Z}_{22}^{(2)} + D_{22}\boldsymbol{Z}_{22}^{(D)} + R_{22}\boldsymbol{Z}_{22}^{(R)} + \boldsymbol{Z}_{22}^{(P)}, \tag{5.7}$$

and solve the resulting homogeneous and non-homogeneous differential problems:

$$\mathscr{L}_{22}\boldsymbol{Z}_{22}^{(1,2)} = 0, \qquad \mathscr{L}_{22}\boldsymbol{Z}_{22}^{(D)} = \boldsymbol{D}_{22}, \qquad \mathscr{L}_{22}\boldsymbol{Z}_{22}^{(R)} = \boldsymbol{R}_{22}, \qquad \mathscr{L}_{22}\boldsymbol{Z}_{22}^{(P)} = \boldsymbol{P}_{22}. \tag{5.8}$$

The boundary conditions at the free surface plus the Exner equation eventually produce the non-homogeneous algebraic system:

$$\boldsymbol{U}_{22}\cdot\boldsymbol{C}_{22} = \boldsymbol{U}_{22}^{(P)}, \qquad \boldsymbol{C}_{22} = \left(c_{22}^{(1)}, c_{22}^{(2)}, D_{22}, R_{22}\right)^T, \tag{5.9}$$

the solution of which determines the unknowns constants $\boldsymbol{C}_{22}$. As for the corresponding linear differential operator, the array $\boldsymbol{U}_{22}$ is obtained from $\boldsymbol{U}_{11}$ substituting k with $2k_c$ while the vector $\boldsymbol{U}_{22}^{(P)}$ is given in Appendix C.†

A slightly different treatment is required to handle the 20 and $20F$ systems, which represent nonlinear distortions of the basic uniform flow arising from the interactions of the fundamental with its complex conjugate and by the perturbations of the Froude number in (5.1), respectively. They can be written as:

$$\mathscr{L}_{20}\boldsymbol{Z}_{20} - D_{20}\boldsymbol{D}_{20} - S_{20}\boldsymbol{S}_{20} = \boldsymbol{P}_{20}, \qquad \mathscr{L}_{20}\boldsymbol{Z}_{20F} - D_{20F}\boldsymbol{D}_{20} - S_{20F}\boldsymbol{S}_{20} = \boldsymbol{P}_{20F}, \tag{5.10}$$

where the linear differential operator $\mathscr{L}_{20}$ is obtained from $\mathscr{L}_{11}$ for vanishing k, while the terms proportional to S_{20} and S_{20F} arise from the perturbation of the gravity term in (2.1). The vectors $\boldsymbol{D}_{20}$, $\boldsymbol{S}_{20}$ and $\boldsymbol{P}_{20F}$ are:

$$\boldsymbol{D}_{20} = -\boldsymbol{I}_{20}, \qquad \boldsymbol{S}_{20} = S_0^{-1}\boldsymbol{I}_{20} \qquad \boldsymbol{P}_{20F} = -2\boldsymbol{I}_{20}, \qquad \boldsymbol{I}_{20} = (0, 0, 1, 0)^T, \tag{5.11}$$

while the vector $\boldsymbol{P}_{20}$, which involves interactions of the fundamental with its complex conjugate, is given in Appendix B.

At this point, it may be useful to point out the kind of experiment implied by (5.1). Since the friction coefficient C is assumed to be held constant, perturbing the Froude number corresponds, owing to (3.5), to a perturbation S_{20F} of the average slope. We are then considering a uniform flow that is slightly perturbed with respect to the critical conditions, preserving the uniform flow depth and depth-averaged velocity and letting the slope adjust according to (3.5). In strict analogy, the interaction of the fundamental with its complex conjugate produces a correction S_{20} proportional to AA^*.

The conservation of the basic unperturbed flow depth and depth-averaged velocity formally corresponds to the imposition of two integral conditions that are automatically satisfied for the systems 11 and 22 and imply, for the systems at hand, that $\overline{U}_{20}$, $\overline{U}_{20F}$, D_{20} and D_{20F} vanish.

We then expand the 20 and $20F$ solutions as:

$$\boldsymbol{Z}_{20} = c_{20}^{(1)}\boldsymbol{Z}_{20}^{(1)} + c_{20}^{(2)}\boldsymbol{Z}_{20}^{(2)} + S_{20}S_0^{-1}\boldsymbol{Z}_{20}^{(I)} + \boldsymbol{Z}_{20}^{(P)}, \tag{5.12}$$

$$\boldsymbol{Z}_{20F} = c_{20F}^{(1)}\boldsymbol{Z}_{20}^{(1)} + c_{20F}^{(2)}\boldsymbol{Z}_{20}^{(2)} + \left(S_{20F}S_0^{-1} - 2\right)\boldsymbol{Z}_{20}^{(I)}, \tag{5.13}$$

† Appendices B and C are available as a supplement to the online version of the paper.

https://doi.org/10.1017/S0022112008002814 Published online by Cambridge University Press

and solve the resulting differential problems:

$$\mathscr{L}_{20}\boldsymbol{Z}_{20}^{(1,2)} = 0, \qquad \mathscr{L}_{20}\boldsymbol{Z}_{20}^{(I)} = \boldsymbol{I}_{20}, \qquad \mathscr{L}_{20}\boldsymbol{Z}_{20}^{(P)} = \boldsymbol{P}_{20}. \tag{5.14}$$

As far as the boundary conditions at the free surface are concerned, we remark that the kinematic boundary condition degenerates and is formally replaced by the integral condition on the depth-averaged velocity. In addition, since the bed neither aggrades nor degrades under uniform flow conditions, the Exner equation does not provide any further information at this order and, without loss of generality, we can safely set $R_{20} = R_{20F} = 0$.

The dynamic boundary conditions at the free surface plus the integral condition on the depth-averaged velocity produce two non-homogeneous algebraic systems, namely:

$$\boldsymbol{U}_{20}\cdot\boldsymbol{C}_{20} = \boldsymbol{U}_{20}^{(P)}, \qquad \boldsymbol{C}_{20} = \left(c_{20}^{(1)}, c_{20}^{(2)}, S_{20}\right)^T, \tag{5.15}$$

$$\boldsymbol{U}_{20}\cdot\boldsymbol{C}_{20F} = \boldsymbol{U}_{20F}^{(I)}, \qquad \boldsymbol{C}_{20F} = \left(c_{20F}^{(1)}, c_{20F}^{(2)}, S_{20F}\right)^T, \tag{5.16}$$

which are readily solved in the unknowns $\boldsymbol{C}_{20}$ and $\boldsymbol{C}_{20F}$. The matrix $\boldsymbol{U}_{20}$ and the vectors $\boldsymbol{U}_{20}^{(P)}$, $\boldsymbol{U}_{20F}^{(I)}$ are given in Appendix C.

5.3. $O(\epsilon^3)$

At third order, the spatial dependence of the fundamental is reproduced and therefore we can write:

$$G_3 = G_{31}\exp[\mathrm{i}k_c(\xi - \Omega_c\tau)] + A^3 G_{33}\exp[3\mathrm{i}k_c(\xi - \Omega_c\tau)] + c.c. \tag{5.17}$$

The related differential systems read:

$$\mathscr{L}_{11}\boldsymbol{Z}_{31} - D_{31}\boldsymbol{D}_{11} - R_{31}\boldsymbol{R}_{11} = \frac{\mathrm{d}A}{\mathrm{d}T}\boldsymbol{P}_{31}^{(1)} + A^2A^*\boldsymbol{P}_{31}^{(3)}, \tag{5.18}$$

$$\mathscr{L}_{33}\boldsymbol{Z}_{33} - D_{33}\boldsymbol{D}_{33} - R_{33}\boldsymbol{R}_{33} = A^3\boldsymbol{P}_{33}, \tag{5.19}$$

where the vectors $\boldsymbol{P}_{31}^{(1,2,3)}$ and $\boldsymbol{P}_{33}$ are functions of η expressed in terms of products of basic- , leading- and second-order components of the perturbations, reported in Appendix A. The linear differential operator $\mathscr{L}_{33}$ is again obtained from $\mathscr{L}_{11}$ substituting k with $3k_c$.

The solution of the 33-system follows the same procedure as outlined in the previous subsection for the 22-system. Once again, the solution is expanded as:

$$\boldsymbol{Z}_{33} = c_{33}^{(1)}\boldsymbol{Z}_{33}^{(1)} + c_{33}^{(2)}\boldsymbol{Z}_{33}^{(2)} + D_{33}\boldsymbol{Z}_{33}^{(D)} + R_{33}\boldsymbol{Z}_{33}^{(R)} + \boldsymbol{Z}_{33}^{(P)}, \tag{5.20}$$

and the solution of the non-homogeneous algebraic system:

$$\boldsymbol{U}_{33}\cdot\boldsymbol{C}_{33} = \boldsymbol{U}_{33}^{(P)}, \qquad \boldsymbol{C}_{33} = \left(c_{33}^{(1)}, c_{33}^{(2)}, D_{33}, R_{33}\right)^T, \tag{5.21}$$

allows for the determination of the constants $\boldsymbol{C}_{33}$. The matrix $\boldsymbol{U}_{33}$ is obtained from $\boldsymbol{U}_{11}$ by replacing k with $3k_c$ and the vector $\boldsymbol{U}_{33}^{(P)}$ is given in Appendix C.

As far as the 31-system is concerned, once the particular solutions $\boldsymbol{Z}_{31}^{(P1,P2,P3)}$ of the non-homogeneous differential systems:

$$\mathscr{L}_{11}\boldsymbol{Z}_{31}^{(P1,P2,P3)} = \boldsymbol{P}_{31}^{(1,2,3)}, \tag{5.22}$$

are obtained, the boundary conditions at the free surface and the Exner equation can be cast in a similar way as (3.13) to give:

$$\boldsymbol{U}_{11}\cdot\boldsymbol{C}_{31} = \frac{\mathrm{d}A}{\mathrm{d}T}\boldsymbol{U}_{31}^{(1)} + AF_2\boldsymbol{U}_{31}^{(2)} + A^2A^*\boldsymbol{U}_{31}^{(3)}, \tag{5.23}$$

https://doi.org/10.1017/S0022112008002814 Published online by Cambridge University Press

where the second term on the right-hand side is generated by the boundary conditions and by the Exner equation.

The homogeneous part of the algebraic system (5.23) admits of a non-trivial solution so that a solvability condition has to be satisfied, which can be found by imposing that the determinant of the matrix obtained by substituting the right-hand side of (5.23) into the last column of $\boldsymbol{U}_{11}$ must vanish. Having set:

$$\delta_i = \det\left(\boldsymbol{U}_{11}^{(i)}\right), \tag{5.24}$$

where the arrays $\boldsymbol{U}_{11}^{(i)}$ are obtained substituting the vector $\boldsymbol{U}_{31}^{(i)}$ into the last column of $\boldsymbol{U}_{11}$, the following Landau–Stuart amplitude equation is readily obtained:

$$\delta_1 \frac{\mathrm{d}A}{\mathrm{d}T} + \delta_2 F_2 A + \delta_3 A^2 A^* = 0. \tag{5.25}$$

After some manipulations, the above equation can be rewritten as:

$$\frac{\mathrm{d}|A|}{\mathrm{d}T} = |A|(\alpha_1 F_2 + \alpha_2 |A|^2), \tag{5.26}$$

where:

$$\alpha_1 = -Re\left(\frac{\delta_2}{\delta_1}\right) \qquad \alpha_2 = -Re\left(\frac{\delta_3}{\delta_1}\right), \tag{5.27}$$

and, from now on, the symbol $\|$ will be omitted for simplicity.

The coefficient α_1 is found to be proportional to the derivative of the imaginary part of the growth rate with respect to the Froude number. In turn, as expressed by (3.12), the growth rate is proportional to the phase-lag between the bed shear stress and the bed itself. Thus, α_1 is a measure of how fast the phase-lag increases with the Froude number in a neighbourhood of critical conditions. On the contrary, a physical explanation of the Landau coefficients α_2 is not readily available.

In light of the following discussion on the results of the weakly nonlinear analysis for the case of dunes and antidunes, it is worth examining briefly the kind of bifurcations that are described by the Landau–Stuart equation (5.26).

If the coefficient α_2 is dropped, an exponential behaviour for $A(T)$ is recovered with $\alpha_1 F_2$ representing the linear growth rate of the perturbation. Nonlinearity, expressed by the coefficient α_2 might inhibit the exponential growth so that an equilibrium amplitude is eventually attained as $T \to \infty$.

Equation (5.26) admits of two steady solutions: the trivial one, $A_1 = 0$, and the solution:

$$A_2 = \sqrt{-\frac{\alpha_1 F_2}{\alpha_2}}. \tag{5.28}$$

For the A_2 solution to exist, the coefficient α_2 must not vanish, a condition that identifies the so-called 'tricritical point', and it must have opposite sign with respect to the product $\alpha_1 F_2$. If α_2 is negative, the bifurcation is termed supercritical and an equilibrium solution is found for positive values of the linear growth rate. On the contrary, when α_2 is positive, the bifurcation is termed subcritical. In this case, the cubic term in (5.26) is unable to balance the linear exponential growth of the perturbations; rather, the A_2 solution exists for perturbations that linearly decay (hence the definition of 'subcritical'). The linear stability of the solutions A_1 and A_2 is readily investigated: the trivial solution is stable for negative values of $\alpha_1 F_2$ and loses stability crossing the bifurcation point $F_2 = 0$; the A_2 solution is always stable when the bifurcation is supercritical and unstable when it is subcritical.

https://doi.org/10.1017/S0022112008002814 Published online by Cambridge University Press

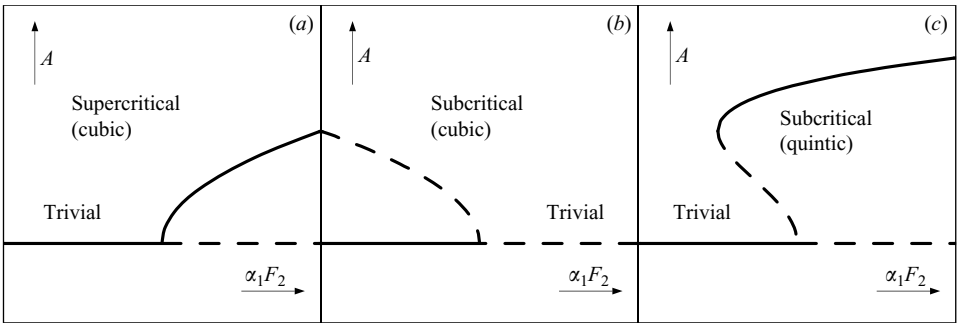


FIGURE 5. Bifurcation diagrams for the Landau–Stuart amplitude equation; solid lines represent stable solutions, dashed lines unstable solution. (*a*) Supercritical bifurcation, cubic equation, $\alpha_2 < 0$. (*b*) Subcritical bifurcation, cubic equation, $\alpha_2 > 0$. (*c*) Subcritical bifurcation, quintic equation, $\alpha_2 > 0$ and $\alpha_3 < 0$.

The bifurcation diagrams for the supercritical and subcritical cases are shown in figures 5(*a*) and 5(*b*), respectively. In the latter case, no stable bifurcating solutions exist beyond $F_2 = 0$, thus implying that the amplitude equation in the form (5.26) is inadequate to describe the nonlinear dynamics of such perturbations. In the subcritical case, the analysis must be pursued to higher order in order to locate the damping mechanism. If a fictitious quintic-order term is added to the amplitude equation as in:

$$\frac{\mathrm{d}A}{\mathrm{d}T} = A(\alpha_1 F_2 + \alpha_2 A^2 + \alpha_3 A^4), \tag{5.29}$$

the subcritical bifurcation diagram changes (figure 5*c*). A stable finite-amplitude solution is now present above the bifurcation point. Moreover, in the interval $\alpha_2^2/(4\alpha_3) < \alpha_1 F_2 < 0$ both, the trivial and the bifurcating solutions are simultaneously stable and can be reached depending on the amplitude of the initial disturbance.

6. Weakly nonlinear theory: discussion of results

We now apply the bifurcation analysis presented in the previous section to the study of dune and antidune instability.

Tricritical points, which mark the change of state of the bifurcation from subcritical to supercritical, exist along both the critical F_{cd} and F_{ca} curves. However, they are found at such extreme values of the dimensionless conductance coefficient ($C = 11$, $f = 0.066$ for antidunes and $C = 24$, $f = 0.014$ for dunes) that, for values of C of practical interest, dune bifurcation can consistently be taken as supercritical whereas antidune bifurcation is subcritical.

Therefore, an equilibrium amplitude can be identified for dune instability while no information can be gathered on antidunes at the present level of approximation. In this respect, a quintic-amplitude equation might be sought to determine a stable asymptotic solution according to the mechanism outlined at the end of the previous section. However, rather than pursuing the weakly nonlinear analysis to the fifth order, the inclusion of suspension into the sediment transport model seems to be the first task to be addressed. In fact, previous stability analyses (Engelund 1970; Engelund & Fredsøe 1974) have shown that a suspended load has a significant influence on antidune development and is therefore potentially capable of modifying

https://doi.org/10.1017/S0022112008002814 Published online by Cambridge University Press

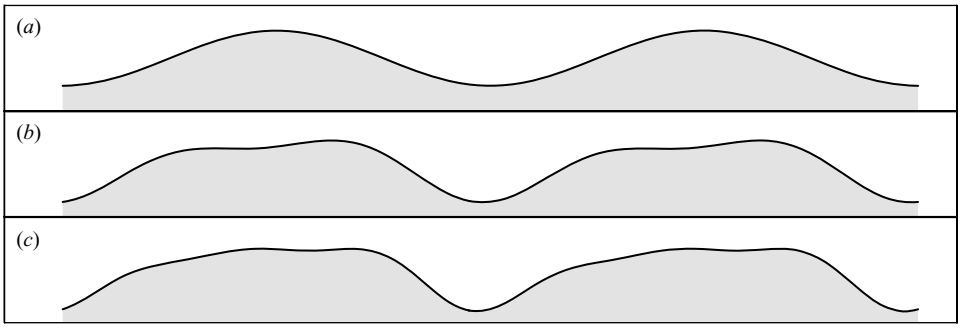


FIGURE 6. Sketch of bottom topography at various orders of approximation in ϵ; (*a*) fundamental; (*b*) effect of second-order terms; (*c*) effect of third-order terms. Vertical scale is enhanced. $C = 22$, $\epsilon = 0.1$.

the linear threshold for antidune instability, the position of the related tricritical point, or both, thus altering the whole bifurcation picture.

Even in bedload dominated context such as the one examined herein, the fact that antidune instability is subcritical suggests a possible explanation for the observed overlapping between upper flow plane bed and antidune solutions (see figure 4 and the related discussion). In fact, close to F_{ca}, both the plane-bed and the antidune solutions could be simultaneously stable. On the contrary, no overlapping exists at F_{cd} between the dune and the upper plane bed regimes since dune instability is supercritical in the range examined.

The supercritical nature of the dune bifurcation allows then for an immediate verification of the results of the weakly nonlinear analysis in terms of shape and amplitude of the bedforms. In fact, for any given set of the model parameters, all variables of the flow-bed system can be reconstructed from (5.3) once the equilibrium amplitude is obtained.

In figure 6, an example of a dune bed profile is shown, where the expansion is truncated at different orders of approximation in ϵ. The shape of the linear wave solution is shown in figure 6(*a*). As the nonlinear $O(\epsilon^2)$ correction is added to the fundamental (figure 6*b*), an asymmetric bed profile is found, with a steeper front and a more gentle slope upstream of the crest. This is due to the action of the R_{22}-component, which leads the fundamental, thus moving the crest downstream. This effect is enhanced by the third-order component R_{33} (figure 6*c*), which also eliminates the kink observed on the stoss side of the dune, producing a more realistic concave profile that becomes almost flat as the dune crest is approached (Allen 1968; Carling *et al.* 2000). Note that the third-order contribution to the bedform amplitude is almost negligible.

The tendency of dunes to create steep fronts as they develop, besides being evident from observations, was substantiated by Reynolds (1965), who suggested that, in general, the steeper faces of bed perturbations are those facing in the direction of motion. The steepening role of the second harmonic has been outlined by Fredsøe (1974) in his analysis of second-order interactions and is recovered here in the formal context of a weakly nonlinear theory.

Following the same procedure, the perturbed flow field up to $O(\epsilon^3)$ is plotted in figure 7, in terms of the streamfunction Ψ, defined in a reference frame moving with

https://doi.org/10.1017/S0022112008002814 Published online by Cambridge University Press

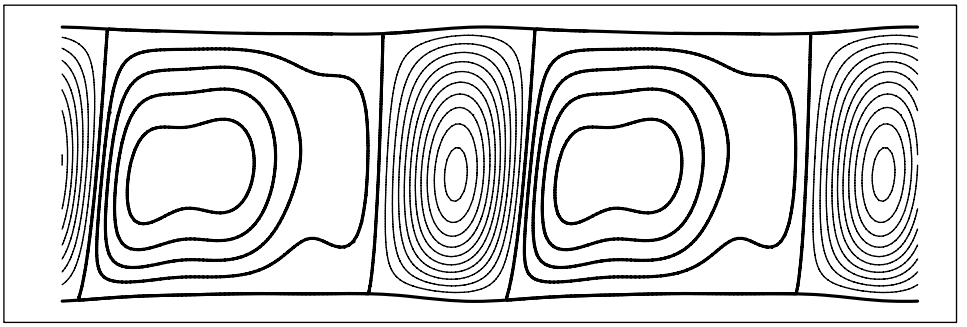


FIGURE 7. Perturbed streamfunction up to $O(\epsilon^3)$. Thicker lines indicate clockwise rotation, thinner lines counterclockwise rotation. $C = 22$, $\epsilon = 0.1$.

the dune celerity as:

$$\frac{\partial \Psi}{\partial y} = U - \Omega_c, \qquad \frac{\partial \Psi}{\partial x} = -V. \tag{6.1}$$

This secondary flow is driven by depth variations, which are generated by the phase shift between the free-surface and the bed oscillations.

Two counter-rotating cells emerge, which reflect the asymmetry of the flow domain since an upwelling flow is found over the dune crests and a downwelling flow over the troughs. This results in a more intense secondary flow downstream of the crest. No recirculating flow is obtained, as expected, in the lee of the dune.

This feature deserves some attention since the role of separation in dune morphodynamics has long been debated (see Best 2005, and references therein). If, on one side, flow separation behind the crest certainly affects the local shear stress distribution and the sediment transport, on the other side, the present results indicate that dunes of finite, though small, height evolve towards an asymmetric shape and reach an equilibrium amplitude even in the absence of flow separation.

The acceleration/deceleration of the flow associated with the sequence of contractions and expansions above the dune is critical in controlling the shape of the bed surface through nonlinear interactions. In particular, the relative amplitude and phase of the R_{22}-component, which are responsible for the asymmetric shape of the dune (see figure 6), are again related to the phase-lag between shear stress and sediment transport that, at linear level, drives the whole instability process.

Finally, a comparison between theoretical predictions and laboratory observations of dune amplitude is presented in figure 8. The theoretical dune height A_t is defined as the difference between the maximum and minimum bed elevations within a dune wavelength, approximated at $O(\epsilon^2)$. We recall that the experimental amplitudes A_e are scaled by the hydraulic radii of the bed region, evaluated by the procedure outlined in § 4.

About one hundred runs relative to fully developed dunes have been extracted from the experimental dataset of Guy *et al.* (1966). Runs cover a wide range of grain sizes (0.19–0.93 mm), Froude numbers (0.25–0.7) and dimensionless conductance coefficients (16–22). Nearly one third of the runs (grey markers in figure 8) are characterized by significant transport in suspension according to the Van Rijn criterion.

The order of magnitude of the bedform amplitudes is captured well by the weakly nonlinear model. Even though data display an appreciable scatter around the line of

https://doi.org/10.1017/S0022112008002814 Published online by Cambridge University Press

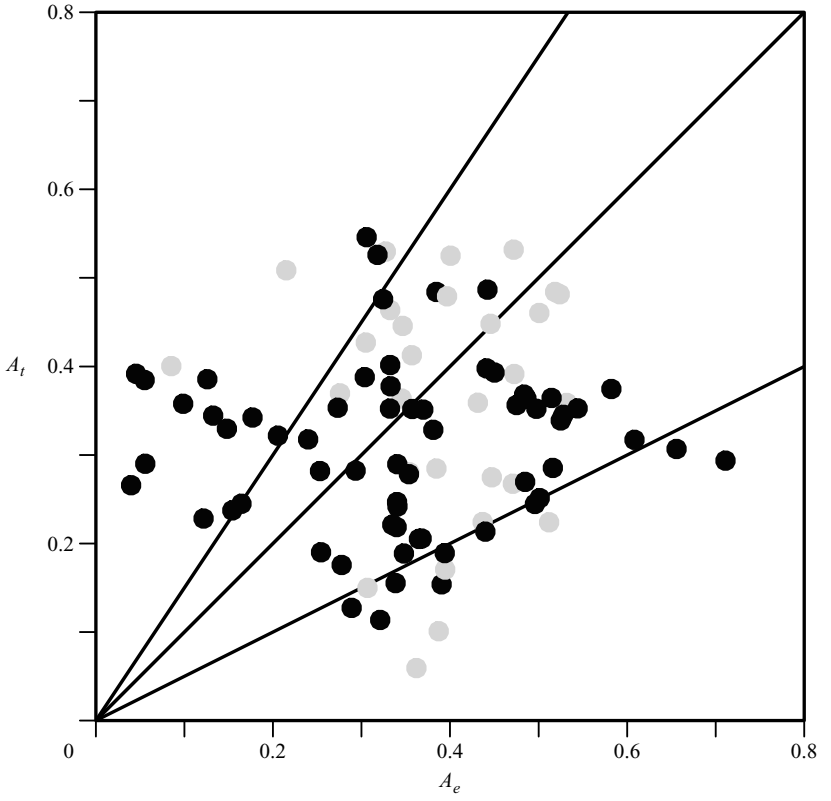


FIGURE 8. Comparison between theoretical (A_t) and experimental (A_e) dune height. Dune experiments of Guy *et al.* (1966).

perfect agreement, about 70 % of them are affected by an error of less than ± 50 %. The largest group of data falling outside of the 50 %-error band, which are sharply overestimated by the theory, refer to conditions quite close to the critical threshold for sediment motion. About this particular set of experiments, the notes of Guy *et al.* (1966) clearly keep track of the low bedload, since not all the sediment moved and the bed was plane except for 'very small' and 'very low' dunes that occurred close to the walls and 'tapered down' to the plane bed.

As far as the theoretical results are concerned, it must be pointed out that the weakly nonlinear solution is expanded in the neighbourhood of the critical point F_{cd}, where the α_1 and α_2 coefficients, and so the equilibrium amplitude A, are evaluated. Hence, as the Froude number is lowered, the theoretical amplitude increases regardless of the approach of the no-motion threshold. Furthermore, the small parameter ϵ increases according to (5.1) and the weakly nonlinear solution becomes less reliable. In this regard, we remark that, for all the data analysed, the maximum values of ϵ do not exceed 0.75. Although the expansion is found to be strictly convergent for $\epsilon \leqslant 0.3$, a satisfactory agreement is displayed in figure 8 even for higher values of ϵ. Moreover, the quantity ϵA is always lower than 0.03, so that the $O(\epsilon^3 A^3)$ corrections, which have been neglected in the evaluation of the theoretical dune amplitude, are reasonably small.

Note that an increase of the amplitude with decreasing Froude number is displayed also by the functional relationship of Van Rijn (1984*b*), which, far from the no-motion

https://doi.org/10.1017/S0022112008002814 Published online by Cambridge University Press

threshold, can be approximated as

$$A_t = K(25 - T), \qquad T = \frac{\theta - \theta_c}{\theta_c}, \qquad \theta = \frac{F^2}{C^2(s-1)d_s}, \tag{6.2}$$

where the constant K depends on the dimensionless grain size d_s.

Finally, no particular differences are detected in the accuracy of the predictions for runs characterized by a relevant suspended sediment transport with respect to bedload only data, an indirect confirmation that dune morphodynamics is only moderately affected by suspension.

7. Conclusions

Dune and antidune instability have been investigated both in the linear and weakly nonlinear regimes. The results of the linear analysis extend those presented in Colombini (2004) and Colombini & Stocchino (2005). In particular, the regions of instability for dunes and antidunes in the $(C - F)$ space have been derived and tested against the experimental dataset of Guy *et al.* (1966). Experimental runs for fully developed dunes fit fairly well into the theoretical regions of instability. The tendency for dunes to disappear as the non-dimensional grain size increases is predicted. On the contrary, the transition from plane bed to antidunes is not satisfactorily described at a linear level, partly because suspended sediment transport has been ignored. A further experimental observation still requiring a sound explanation is the absence of a net separation between upper flow plane bed solutions and antidunes, at least for Froude numbers below 1.2. The present approach suggests that a hysteresis loop might occur. In fact, the bifurcation analysis performed in the weakly nonlinear context shows that antidune bifurcation is subcritical in character. However, a conclusive answer in this regard cannot be sought within the present formulation since a higher-order bifurcation analysis would be required.

On the contrary, dune instability is found to be consistently supercritical and this allows for the determination of an equilibrium amplitude.

Bed perturbations display, as they grow, a tendency to form steeper lee fronts and milder stoss sides. For small values of the parameter ϵ, the theoretical bed profile at equilibrium reproduces well the main geometrical features of low-amplitude dunes. The present theory can therefore describe finite-amplitude dune growth when the steepness of the front at equilibrium remains small enough to prevent flow separation at the crest. In this case, the phase-lag between flow and bed topography is confirmed to be the mechanism controlling dune formation and nonlinear evolution. Moreover, a satisfactory agreement between theoretical predictions and laboratory observations of dune height is found, which suggests that the present weakly nonlinear model can provide a rough estimate of dune amplitude even for larger values of ϵ (i.e. for larger steepnesses), although the question of how separation affects dune development as the steepness of the front increases remains open.

We are fully aware that our results provide a simplified representation of the flow and sediment transport over dunes, as it emerges from laboratory and field observations. This is partly due to the intrinsic limitations of the perturbative approach adopted. In fact, convergence of the power expansion (5.3) is ensured only in a neighbourhood of the critical conditions. Moreover, separation in the leeside of the dune can be handled satisfactorily only by means of a fully nonlinear numerical solution. On the other hand, the present analysis could be extended to include further effects that might be relevant in order to improve the overall description

https://doi.org/10.1017/S0022112008002814 Published online by Cambridge University Press

of the phenomenon. In this regard, some suggestions have already been mentioned throughout the paper. Among others, the inclusion of suspension and the analysis of wave-packet evolution seem to be the most promising.

Nonetheless, in spite of these limitations, we feel that a further step has been taken in the direction of a predictive theory for dune and antidune finite-amplitude evolution, which could eventually lead to a rational estimate of dune height in terms of the main flow and sediment parameters. In particular, we hope that the present work may contribute to addressing at least a few of the many challenging questions raised by the ASCE Task Committee on Flow and Transport over Dunes (ASCE 2002).

This research has been partially supported by the Fondazione Cassa di Risparmio di Verona, Vicenza, Belluno ed Ancona (Project MODITE).

Appendix A

The linear differential operator $\mathscr{L}_{11}$ in (3.8) is:

$$\mathscr{L}_{11} = \begin{pmatrix} \mathrm{d}/\mathrm{d}\eta & \mathrm{i}k/2 & -1/(2\nu_{T0}) & 0 \\ \mathrm{i}k & \mathrm{d}/\mathrm{d}\eta & 0 & 0 \\ U_0^{\Omega} - 4k^2\nu_{T0} & -U_0' & \mathrm{d}/\mathrm{d}\eta & \mathrm{i}k \\ 0 & U_0^{\Omega} & \mathrm{i}k & \mathrm{d}/\mathrm{d}\eta \end{pmatrix} \tag{A 1}$$

while the vectors $\boldsymbol{D}$ and $\boldsymbol{R}$ are, respectively:

$$\boldsymbol{D}_{11} = \begin{pmatrix} 0 \\ \mathrm{i}kU_0'\eta \\ U_0^{\Omega}U_0'\eta - 2k^2\eta(1-\eta) - 1 \\ \mathrm{i}k\eta - 2\mathrm{i}k(1-\eta) \end{pmatrix} \qquad \boldsymbol{R}_{11} = \begin{pmatrix} 0 \\ \mathrm{i}kU_0' \\ U_0^{\Omega}U_0' - 2k^2(1-\eta) \\ \mathrm{i}k \end{pmatrix} \tag{A 2}$$

where $U_0^{\Omega} = -\mathrm{i}k(U_0 - \Omega)$ and primes stand for derivatives with respect to η.

The array $\boldsymbol{U}_{11}$ in (3.13) is equal to:

$$\begin{pmatrix} \begin{bmatrix} V_{11}^{(1)} & V_{11}^{(2)} & V_{11}^{(D)} + U_0^{\Omega} & V_{11}^{(R)} + U_0^{\Omega} \\ T_{t11}^{(1)} & T_{t11}^{(2)} & T_{t11}^{(D)} & T_{t11}^{(R)} \\ T_{n11}^{(1)} & T_{n11}^{(2)} & T_{n11}^{(D)} + S_0^{-1} & T_{n11}^{(R)} + S_0^{-1} \end{bmatrix}_1 \\ \begin{bmatrix} T_{t11}^{(1)} & T_{t11}^{(2)} & T_{t11}^{(D)} & T_{t11}^{(R)} - \frac{\Omega F_0}{Q\theta_{r0}} - \frac{\mathrm{i}k\mu}{\theta_{r0}} \end{bmatrix}_{\eta_b} \end{pmatrix}. \tag{A 3}$$

REFERENCES

Allen, J. R. L. 1968 *Current Ripples: Their Relation to Patterns of Water and Sediment Motion*. North-Holland.

ASCE, Task Committee 1963 Friction factors in open channels. *J. Hydraul. Div.* **89** (HY2), 97–143.

ASCE, Task Committee 2002 Flow and transport over dunes. *J. Hydraul. Engng. ASCE* **127**, 726–728.

Besio, G., Blondeaux, P. & Vittori, G. 2006 On the formation of sand waves and sand banks. *J. Fluid Mech.* **557**, 1–27.

Best, J. 2005 The fluid dynamics of river dunes: a review and some future research directions. *J. Geophys. Res. Earth Surface* **110**, F04S02.

Best, J. & Kostaschuk, R. 2002 An experimental study of turbulent flow over a low-angle dune. *J. Geophys. Res. Earth Surface* **107** (C9), 3135–3153.

https://doi.org/10.1017/S0022112008002814 Published online by Cambridge University Press

Blondeaux, P. 1990 Sand ripples under sea waves. Part 1. Ripple formation. *J. Fluid Mech.* **218**, 1–17.

Blondeaux, P. & Seminara, G. 1985 A unified bar-bend theory of river meanders. *J. Fluid Mech.* **157**, 449–470.

Callander, R. A. 1969 Instability and river channels. *J. Fluid Mech.* **36**, 465–480.

Carling, P. A. & Shvidchenko, A. B. 2002 A consideration of the dune:antidune transition in fine gravel. *Sedimentology* **49**, 1269–1282.

Carling, P. A., Gölz, E., Orr, H. G. & Radecki-Pawlik, A. 2000 The morphodynamics of fluvial sand dunes in the river Rhine, near Mainz, Germany. I. sedimentology and morphology. *Sedimentology* **47**, 227–252.

Carling, P. A., Richardson, K. & Ikeda, H. 2005 A flume experiment on the development of subacqueous fine-gravel dunes from a lower-stage plan bed. *J. Geophys. Res. Earth Surface* **110**, F04S05.

Coleman, S. E. & Fenton, J. D. 2000 Potential-flow instability theory and alluvial stream bed forms. *J. Fluid Mech.* **418**, 101–117.

Coleman, S. E. & Melville, B. W. 1996 Initiation of bed forms on a flat sand bed. *J. Hydraul. Engng ASCE* **122**, 301–310.

Coleman, S. E., Nikora, V. I., McLean, S. R., Clunie, T. M., Schlicke, T. & Melville, B. W. 2006 Equilibrium hydrodynamics concept for developing dunes. *Phys. Fluids* **18**, 12.

Colombini, M. 2004 Revisiting the linear theory of sand dune formation. *J. Fluid Mech.* **502**, 1–16.

Colombini, M. & Stocchino, A. 2005 Coupling or decoupling bed and flow dynamics: fast and slow sediment waves at high Froude numbers. *Phys. Fluids* **17** (3), 9.

Colombini, M., Seminara, G. & Tubino, M. 1987 Finite-amplitude alternate bars. *J. Fluid Mech.* **181**, 213–232.

Engelund, F. 1970 Instability of erodible beds. *J. Fluid Mech.* **42**, 225–244.

Engelund, F. & Fredsøe, J. 1974 Transition from dunes to plane bed in alluvial channels. Series paper 4. Tech. Univ. Denmark, Inst. Hydrodyn. and Hydraulic Engng.

Engelund, F. & Hansen, E. 1967 *A Monograph on Sediment Transport in Alluvial Streams*. Teknisk Forlag, Copenhagen, Denmark.

Federici, B. & Seminara, G. 2003 On the convective nature of bar instability. *J. Fluid Mech.* **487**, 125–145.

Fredsøe, J. 1974 On the development of dunes in erodible channels. *J. Fluid Mech.* **64**, 1–16.

Giri, S. & Shimizu, Y. 2006 Numerical computation of sand dune migration with free surface flow. *Water Resour. Res.* **42**, W10422.

Guy, H. P., Simons, D. B. & Richardson, E. V. 1966 Summary of alluvial channel data from flume experiments 1956–61. Prof. paper 462-I. US Geol. Survey.

Ikeda, S., Parker, G. & Saway, K. 1981 Bend theory of river meanders. Part 1. Linear development. *J. Fluid Mech.* **112**, 363–377.

Ji, Z.-G. & Mendoza, C. 1997 Weakly nonlinear stability analysis for dune formation. *J. Hydraul. Engng ASCE* **123**, 979–985.

Kennedy, J. F. 1963 The mechanism of dunes and antidunes in erodible-bed channels. *J. Fluid Mech.* **16**, 521–544.

Lee, H.-Y. & Hsu, I.-S. 1994 Investigation of saltating particle motion. *J. Hydraul. Engng ASCE* **120**, 831–845.

Meyer-Peter, E. & Müller, R. 1948 Formulas for bed-load transport. In *Proc. 2nd Meeting IAHR*, pp. 39–64. Stockholm, Sweden.

Parker, G. 1975 Sediment inertia as cause of river antidunes. *J. Hydraul. Div.* **101**, 536–558.

Reynolds, A. J. 1965 Waves on an erodible bed. *J. Fluid Mech.* **22**, 113–133.

Richards, K. J. 1980 The formation of ripples and dunes on an erodible bed. *J. Fluid Mech.* **99**, 597–618.

Rouse, H. 1946 *Elementary Mechanics of Fluids*. Wiley.

Schielen, R., Doelman, A. & de Swart, H. E. 1993 On the nonlinear dynamics of free bars in straight channels. *J. Fluid Mech.* **252**, 325–356.

Sekine, M. & Kikkawa, H. 1992 Mechanics of saltating grains. *J. Hydraul. Engng ASCE* **118**, 536–558.

https://doi.org/10.1017/S0022112008002814 Published online by Cambridge University Press

Smith, J. D. 1970 Stability of a sand bed subjected to a shear flow at low Froude number. *J. Geophys. Res.* **75**, 5928–5940.

Stuart, J. T. 1971 Nonlinear stability theory. *Annu. Rev. Fluid Mech.* **3**, 347–370.

Sumer, B. M. & Bakioglu, M. 1984 On the formation of ripples on an erodible bed. *J. Fluid Mech.* **144**, 177–190.

Tjerry, S. & Fredsøe, J. 2005 Calculation of dune morphology. *J. Geophys. Res. Earth Surface* **110**, F04013.

Van Rijn, L. C. 1984*a* Sediment transport, Part ii: Suspended load transport. *J. Hydraul. Engng ASCE* **110**, 1613–1641.

Van Rijn, L. C. 1984*b* Sediment transport, Part iii: Bed forms and alluvial roughness. *J. Hydraul. Engng ASCE* **110**, 1733–1754.

Vanoni, V. A. & Brooks, N. H. 1957 Laboratory studies of the roughness and suspended load of alluvial streams. *Tech. Rep.* California Institute of Technology, Pasadena, California.

Wong, M. & Parker, G. 2006 Reanalysis and correction of bed-load relation of Meyer-Peter and Müller using their own database. *J. Hydraul. Engng ASCE* **132**, 1159–1168.

https://doi.org/10.1017/S0022112008002814 Published online by Cambridge University Press